Polarimetric Ground and Volume Decomposition Based on the PolInSAR Two-Layer Model

Alberto Alonso-González, *Member, IEEE*, Noelia Romero-Puig, *Member, IEEE*, Carlos López-Martínez, *Senior Member, IEEE*, and Konstantinos P. Papathanassiou, *Fellow, IEEE*

***Abstract*—This work introduces a methodology to decompose the ground and volume scattering contributions using polarimetric interferometric synthetic aperture radar (PolInSAR) acquisitions. The introduction of interferometric information allows to overcome the limitation of conventional polarimetric model-based decompositions and to obtain full-rank polarimetric coherency matrices for the ground and volume scattering contributions. This is achieved by establishing a link between polarimetric and interferometric measurements in the context of a two-layer model. Assuming that these two dimensions of the data are separable, the polarimetric response of the two layers may be obtained as a function of their interferometric coherences. The proposed approach is applicable to single-baseline as well as multibaseline PolInSAR data. Accordingly, the technique is applied and evaluated with real single-baseline and multibaseline PolInSAR data at P-band and L-band acquired by the German Aerospace Center (DLR)'s F-synthetic aperture radar (SAR) airborne sensor over a tropical forest from the AfriSAR 2016 campaign. Experimental results demonstrate the effectiveness of the proposed decomposition, which provides a uniform high-entropy volume component, while the retrieved ground layer preserves topographic features consistent with the expected polarimetric orientation angle (POA). The analysis confirms the capability of the method to retrieve full-rank component matrices without imposing polarimetric constraints on the scattering mechanisms.**

***Index Terms*—Polarimetric interferometric synthetic aperture radar (PolInSAR), polarimetric synthetic aperture radar (PolSAR) interferometry, polarimetry, synthetic aperture radar (SAR), two-layer model.**

I. Introduction

POLARIMETRIC synthetic aperture radar (PolSAR) data allows to assess the geometric and dielectric properties of scatterers by exploiting the vectorial nature of the electromagnetic waves. PolSAR systems employ orthogonal polarizations in transmission and reception to characterize the polarization dependence of the scattering process [1]. As a result, PolSAR data are used for the estimation of geophysical and biophysical parameters of the scene [2], [3]. In addition to quantitative parameter estimation, PolSAR data have been used to decompose complex scattering processes into simpler or elementary contributions that can either be used as a whole to interpret these complex scattering interactions or to isolate individual scattering contributions that are then used for quantitative parameter estimation [4], [5], [6], [7], [8]. However, polarimetric decomposition approaches are critically limited by the fact that the number of independent measurements provided by PolSAR observations is rather small. This limits the number and/or complexity of the individual scattering contributions that can be used to decompose the scattering process, leading to a loss of information content about such scatterers.

A way to overcome these limitations has emerged through the combination of polarimetry and interferometry. Indeed, interferometric synthetic aperture radar (SAR) measurements with angular diversity (e.g., across-track InSAR) are sensitive to the vertical distribution of scatterers and allow to separate surface scatterers (e.g., scatterers with very limited or even Dirac-like vertical extent) from volume scatterers (e.g., scatterers with vertical extent) [9]. Coherent polarimetric interferometric SAR (PolInSAR) scattering models based on two layers, corresponding to the ground and the vegetation, have been used traditionally to extract forest and agriculture biophysical parameters. Examples of these PolInSAR models are, for instance, the random volume over ground (RVOG) [10] or the interferometric water cloud model (IWM) [11]. These models describe the observed interferometric coherences, and they may be used to invert physical parameters, like the vegetation height or the extinction coefficient.

Although these PolInSAR models may be used to get reliable information about the vertical reflectivity profile, they do not provide direct information about the polarimetry of the involved layers. This type of information would be very useful for a detailed analysis of the temporal evolution of crops and forest or for detecting structural and environmental changes. Some studies have tried to shed some light in this direction by extending the same concept employed in these PolInSAR models to get additional information about the ground or volume components. The concept of the negative alpha filter, for instance, was introduced in [12] in order to get information about the ground below a vegetation layer. Other approaches

Received 29 July 2025; revised 20 January 2026 and 29 April 2026; accepted 26 May 2026. Date of publication 5 June 2026; date of current version 16 June 2026. This work was supported by MCIN/AEI/10.13039/501100011033/FEDER, UE, under Project PID2023-149659OB-C22. *(Corresponding author: Alberto Alonso-González.)*

Alberto Alonso-González is with the Signal Theory and Communications Department, Universitat Politècnica de Catalunya (UPC), 08034 Barcelona, Spain (e-mail: alberto.alonso-gonzalez@upc.edu).

Noelia Romero-Puig and Konstantinos P. Papathanassiou are with the Microwaves and Radar Institute, German Aerospace Center (DLR), 82234 Weßling, Germany.

Carlos López-Martínez is with the Signal Theory and Communications Department, Universitat Politècnica de Catalunya (UPC), 08034 Barcelona, Spain, and also with the Institut d'Estudis Espacials de Catalunya (IEEC), 08034 Barcelona, Spain.

Digital Object Identifier 10.1109/TGRS.2026.3700682

have tried to expand the polarimetric decomposition models to PolInSAR, as in [13] and [14], where the same concept of the Freeman–Durden decomposition has been employed to PolInSAR data.

Alternative approaches derived from SAR tomography have also tried to tackle the layer separation problem from a different perspective. In [15] and [16], the coherency matrix of SAR tomographic data was decomposed into a sum of Kronecker products (SKP). An estimation process was also proposed based on the least-squares approximation by a Kronecker product decomposition [17]. The SKP assumption implies the separability between polarimetry and interferometry aspects of the data, as it is also assumed in many PolInSAR physical models. The least-squares approximation process, however, obtains solutions that do not necessarily fit the classical interpretation of the vertical reflectivity profiles employed in PolInSAR models as, for instance, the ground delta assumption. Although this might have some advantages, as it does not imply any assumption on the vertical reflectivity profile, it complicates the physical interpretation of the obtained components. Moreover, this inversion process is not unique, leading to different solutions equally valid which require additional constraints [15]. Other approaches have tried to circumvent some of these limitations by proposing a hybrid decomposition approach [18], where a physical model is imposed for the ground component while the volume is approximated from the data. An indirect way to analyze one of the two components is to apply polarimetric or interferometric models to cancel the response of one specific layer. This idea has been employed to improve the estimation of underlying topography [19] and also to estimate the volume only response by canceling the ground signal [20]. It is worth mentioning, however, that although the ground response is removed in [20], the obtained volume component is also modulated depending on its vertical reflectivity profile. Similar ideas have been explored in the context of SKP-based decompositions. In particular, Zeng et al. [21] established a relationship between the interferometric structure and polarimetric matrices by expressing the structure matrix as a function of fixed polarimetric responses for the ground and volume components. Although this approach improves the estimation of structure matrices for digital terrain model (DTM) and canopy height model (CHM) retrieval, fixing the polarimetric responses inherently limits the exploitation of the remaining polarimetric diversity for decomposition purposes, especially in complex scattering scenarios.

Therefore, different strategies have been proposed to address the ground and volume separation problem with PolInSAR and tomography. Algebraic approaches, as those based on the SKP, provide a mathematical separation of the contributions, offering additional degrees of freedom that do not necessarily adhere to specific vertical structures. Conversely, physical model-based approaches typically apply some constraints to the solution space by fixing or canceling specific polarimetric responses. As a consequence, there is an interest in exploring methodologies based on the two-layer model to separate ground and volume contributions while preserving the full polarimetric information of both layers without imposing specific scattering mechanisms.

In this work, a direct analytical relationship expressing the polarimetric response of the ground and volume layers as a function of their corresponding interferometric coherences is established within the framework of the PolInSAR two-layer model. This allows setting up a framework for the decomposition of ground and volume scattering contributions using polarimetric interferometric measurements. Unlike other target decomposition approaches, the proposed method does not impose a priori constraints on the polarimetric scattering mechanisms. Instead, the separation exploits the interferometric information of the PolInSAR two-layer model. This allows for the retrieval of general, full-rank polarimetric coherency matrices for both layers.

II. PolInSAR Two-Layer Model

Multibaseline PolInSAR configurations measure the scattering matrix $\mathbf{S}$ [22] for each resolution cell at N different across-track baselines. For the basline i, the scattering vector in the Pauli basis $\mathbf{k}_i$ [4] may be expressed as

$$\mathbf{k}_i = \frac{1}{\sqrt{2}}\left[S^i_{hh} + S^i_{vv},\ S^i_{hh} - S^i_{vv},\ S^i_{hv} + S^i_{vh}\right]^T \tag{1}$$

where S^i_{pq} represents the complex scattering coefficient for $p, q \in [h, v]$ received and transmitted polarization combination, h and v stand for horizontal and vertical polarizations, respectively, and ^{T} stands for vector transpose.

The multibaseline scattering vector $\mathbf{k}$ may be obtained by concatenation of all the $\mathbf{k}_i$ scattering vectors

$$\mathbf{k} = \left[\mathbf{k}_1^T \mathbf{k}_2^T \cdots \mathbf{k}_N^T\right]^T. \tag{2}$$

If the number of individual scattering elements within the resolution cell is sufficiently large, that is, in a distributed scattering scenario, then the central limit theorem applies [23]. In this case, $\mathbf{k}$ becomes a zero-mean complex Gaussian distributed vector that may be completely characterized by the multipolarization multibaseline coherency matrix $\mathbf{Z}_N$

$$\mathbf{Z}_N = E\left\{\mathbf{k}\ \mathbf{k}^H\right\} = \begin{pmatrix} \mathbf{T}_{11} & \boldsymbol{\Omega}_{12} & \cdots & \boldsymbol{\Omega}_{1N} \\ \boldsymbol{\Omega}_{12}^H & \mathbf{T}_{22} & \cdots & \boldsymbol{\Omega}_{2N} \\ \vdots & \vdots & \ddots & \vdots \\ \boldsymbol{\Omega}_{1N}^H & \boldsymbol{\Omega}_{2N}^H & \cdots & \mathbf{T}_{NN} \end{pmatrix} \tag{3}$$

where ^{H} represents the complex Hermitian transpose, $E\{\}$ denotes the statistical expectation, $\mathbf{T}_{ii}$ are the polarimetric coherency matrices for acquisition i and $\boldsymbol{\Omega}_{ij}$ the PolInSAR matrices between i and j acquisitions.

The interferometric coherence γ_{ij} between acquisition i and j for a particular polarization state $\mathbf{w}$ [9] may be expressed as

$$\gamma_{ij}(\mathbf{w}) = \frac{\mathbf{w}^H \boldsymbol{\Omega}_{ij} \mathbf{w}}{\sqrt{\mathbf{w}^H \mathbf{T}_{ii} \mathbf{w} \cdot \mathbf{w}^H \mathbf{T}_{jj} \mathbf{w}}}. \tag{4}$$

This interferometric coherence $\gamma_{ij}(\mathbf{w})$ can be decomposed into a product of several contributions. These include decorrelation due to nonideal SAR system and processing implementations, different scatterers phase under distinct acquisitions geometry, or geometric and dielectric changes of the scatterers in the time between the two acquisitions [24], [25]. In the following, it will be assumed that $\gamma_{ij}(\mathbf{w})$ expresses

only the volume decorrelation term [11], which represents the coherence loss due to volume scattering in vegetated areas:

$$\gamma_{ij}(\mathbf{w}) = \frac{\int \sigma^0(z,\mathbf{w})\, e^{jk_{z_{ij}}z}\, dz}{\int \sigma^0(z,\mathbf{w})\, dz} \tag{5}$$

where $\sigma^0(z,\mathbf{w})$ represents the vertical reflectivity profile as a function of height (z) and polarization ($\mathbf{w}$) and $k_{z_{ij}}$ is the vertical (interferometric) wavenumber between acquisitions i and j. It is defined, for the monostatic case, as

$$k_{z_{ij}} = \frac{4\pi}{\lambda}\frac{\Delta\theta_{ij}}{\sin(\theta_0)} \tag{6}$$

where θ_0 is the nominal incidence angle, λ is the wavelength, and $\Delta\theta_{ij}$ is the change of incidence angle induced by the across-track baseline between acquisition i and j.

A. Two-Layer Model

According to the two-layer model, the scattering may be decomposed into two main contributions represented by two vertically adjacent layers. For a vegetation scenario, the two layers correspond to the volume (top) and ground (bottom) scattering components. Under this assumption, the scattering may be expressed as

$$\sigma^0(z,\mathbf{w}) = \sigma^0_g(z,\mathbf{w}) + \sigma^0_v(z,\mathbf{w}) \tag{7}$$

$$\simeq P_g(\mathbf{w})\, F_g(z) + P_v(\mathbf{w})\, F_v(z) \tag{8}$$

where the subindexes g and v represent the ground and volume components, respectively, $P_l(\mathbf{w})$ represents the total scattering power of each layer $l \in [g,v]$ at polarization state $\mathbf{w}$, and $F_l(z)$ is the normalized vertical reflectivity profile such that $\int F_l(z)dz = 1$.

Introducing (8) into (5), the interferometric coherence between acquisition i and j may be approximated as

$$\widetilde{\gamma}_{ij}(\mathbf{w}) = \frac{P_v(\mathbf{w})\,\gamma^v_{ij} + P_g(\mathbf{w})\,\gamma^g_{ij}}{P_v(\mathbf{w}) + P_g(\mathbf{w})} \tag{9}$$

$$= \frac{\gamma^v_{ij} + \mu(\mathbf{w})\,\gamma^g_{ij}}{1+\mu(\mathbf{w})} \tag{10}$$

where the tilde in $\widetilde{\gamma}_{ij}(\mathbf{w})$ represents the observations modeled according to the two-layer assumption and γ^g_{ij} and γ^v_{ij} represent the ground and volume interferometric coherences, defined as

$$\gamma^l_{ij} = \int F_l(z)\, e^{jk_{z_{ij}}z}\, dz \tag{11}$$

with $l \in [g,v]$ representing the layer, and $\mu(\mathbf{w})$ is the ground to volume ratio

$$\mu(\mathbf{w}) = \frac{P_g(\mathbf{w})}{P_v(\mathbf{w})}. \tag{12}$$

The approximation in (8) encapsulates the main assumption of the two-layer model: the normalized vertical profiles $F_g(z)$ and $F_v(z)$ are independent of $\mathbf{w}$, making the ground and volume coherences γ^g_{ij} and γ^v_{ij} independent of the polarization state. This assumption is also referred to as *random volume*, in contrast to *oriented volume*, where different volume profiles are assumed for different polarization states.

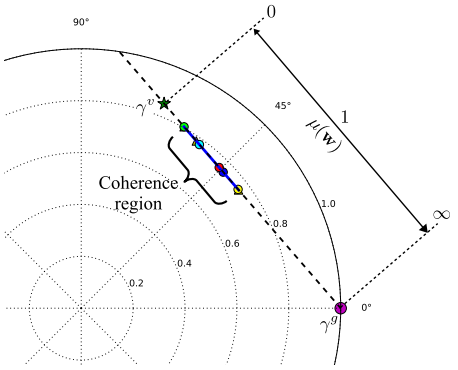

Fig. 1. Coherence region for the two-layer model on the complex plane. A segment of the line between γ^g and γ^v is obtained according to $\mu(\mathbf{w})$ values.

The two-layer model assumption in (8) also allows to define the polarimetric coherency $\widetilde{\mathbf{T}}_{ii}$ and PolInSAR $\widetilde{\mathbf{\Omega}}_{ij}$ matrices in (3) according to the two-layer model, as already noted in [26] and [27], as

$$\widetilde{\mathbf{T}}_{ii} = \mathbf{T}_g + \mathbf{T}_v \tag{13}$$

$$\widetilde{\mathbf{\Omega}}_{ij} = \gamma^g_{ij}\mathbf{T}_g + \gamma^v_{ij}\mathbf{T}_v \tag{14}$$

where $\mathbf{T}_g$ and $\mathbf{T}_v$ are the polarimetric coherency matrices of the ground and volume components, respectively, and γ^g_{ij} and γ^v_{ij} represent their interferometric coherences, defined in (11). It is worth to note that with this definition the ground and volume powers in (8)–(12) may be obtained as

$$P_g(\mathbf{w}) = \mathbf{w}^H\mathbf{T}_g\mathbf{w} \tag{15}$$

$$P_v(\mathbf{w}) = \mathbf{w}^H\mathbf{T}_v\mathbf{w}. \tag{16}$$

According to the described two-layer model, the multibaseline coherency matrix $\mathbf{Z}_N$ may be approximated by an SKP, as described in [15], by applying (13) and (14) into (3)

$$\widetilde{\mathbf{Z}}_N = \mathbf{R}_g \otimes \mathbf{T}_g + \mathbf{R}_v \otimes \mathbf{T}_v \tag{17}$$

where $\widetilde{\mathbf{Z}}_N$ represents the two-layer model approximation of $\mathbf{Z}_N$, and $\mathbf{R}_g$ and $\mathbf{R}_v$ are the $N \times N$ positive semidefinite structure matrices of the ground and volume, respectively. They contain ones on the diagonal and the coherences (γ^g_{ij} and γ^v_{ij}) in the off-diagonal elements

$$\mathbf{R}_l = \begin{pmatrix} 1 & \gamma^l_{12} & \cdots & \gamma^l_{1N} \\ \gamma^{l*}_{12} & 1 & \cdots & \gamma^l_{2N} \\ \vdots & \vdots & \ddots & \vdots \\ \gamma^{l*}_{1N} & \gamma^{l*}_{2N} & \cdots & 1 \end{pmatrix}, \quad \text{for } l \in (g,v). \tag{18}$$

B. Coherence Linearity

As it may be seen in (10), under the two-layer model assumption previously described, the set of all possible coherences for different polarization states $\widetilde{\gamma}_{ij}(\mathbf{w})$, also known as *coherence region* [28], is a line segment between the two-layer coherences γ^g_{ij} and γ^v_{ij}, bounded by the ground to volume ratio $\mu(\mathbf{w})$ values [10]. This line and the coherence region line segment are represented in Fig. 1. In general, distinct two-layer models differ in the interpretation of these layers or in the

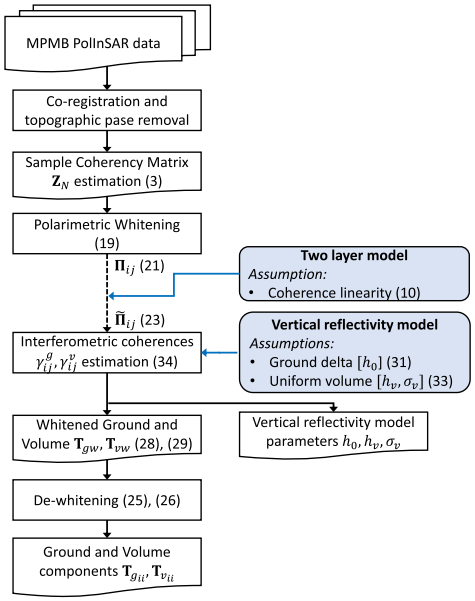

Fig. 2. Block diagram of the proposed method. Modeling assumptions are highlighted in blue color.

definition of their vertical characteristics $F_l(z)$. The coherence linearity, however, is always obtained (given the mentioned assumption) regardless of the employed vertical reflectivity profile. Therefore, assuming the PolInSAR two-layer model, the observed coherence region $\gamma_{ij}(\mathbf{w})$ can be geometrically interpreted as a line segment. This interpretation is essential for deriving the ground and volume decomposition, as discussed in Section III.

The coherence linearity has been observed in a wide range of scenarios, including forest and vegetation in general, especially at lower frequencies like P-band and L-band [3]. Moreover, the validity of this assumption, as introduced in (13) and (14), may be tested with statistical tests [27] or approximation error measures [26].

III. Ground and Volume Response Decomposition

The block diagram of the proposed method is shown in Fig. 2, where different modeling assumptions are clearly highlighted in blue color. As it may be seen, the proposed technique is based on the two-layer model and coherence linearity previously explained in Section II.

Equations (13) and (14) allow to extract the ground and volume polarimetric coherency matrices $\mathbf{T}_g$ and $\mathbf{T}_v$ from the ground and volume interferometric coherences γ_{ij}^g and γ_{ij}^v. According to (13), the polarimetric $\widetilde{\mathbf{T}}_{ii}$ matrices should be equal for all the acquisitions. This is a consequence of the assumption that layer components, $P_g(\mathbf{w})$ and $P_v(\mathbf{w})$, are constant for all the acquisitions. However, this is not generally the case in real data, as small differences may be observed due to speckle and other noise sources. Some approaches try to achieve the ground and volume components that *best approximate* all the $\mathbf{Z}_N$ elements based on some metric, like the Frobenius norm [15], [18]. In this article, the ground and volume separation is defined as a decomposition problem where the polarimetric coherency matrix $\mathbf{T}_{ii}$ of each acquisition is exactly decomposed into two components such that $\mathbf{T}_{ii} = \mathbf{T}_{g_{ii}} + \mathbf{T}_{v_{ii}}$, removing the approximation $\widetilde{\mathbf{T}}_{ii}$ in (13). To achieve this, a polarimetric whitening is applied, and the assumption of constant ground and volume components between acquisitions is moved to the whitened space, as can be seen in Fig. 2.

A. Polarimetric Whitening

A polarimetric whitening filter is first applied to the data to effectively project it into a normalized observation space common to all acquisitions. This serves two main purposes: 1) to compensate for polarimetric variability between baselines due to slight differences in the $\mathbf{T}_{ii}$ matrices and 2) to achieve an exact separation of ground and volume components through total power normalization, ensuring the preservation of total backscattering energy. In the most general case, for the multi-baseline coherency matrix $\mathbf{Z}_N$ defined in (3), the polarimetric whitening is expressed as

$$\mathbf{Z}_w = \mathbf{N}_T^{-\frac{1}{2}} \mathbf{Z}_N \mathbf{N}_T^{-\frac{1}{2}} = \begin{pmatrix} \mathbf{I} & \mathbf{\Pi}_{12} & \cdots & \mathbf{\Pi}_{1N} \\ \mathbf{\Pi}_{12}^H & \mathbf{I} & \cdots & \mathbf{\Pi}_{2N} \\ \vdots & \vdots & \ddots & \vdots \\ \mathbf{\Pi}_{1N}^H & \mathbf{\Pi}_{2N}^H & \cdots & \mathbf{I} \end{pmatrix} \tag{19}$$

$$\mathbf{N}_T = \begin{pmatrix} \mathbf{T}_{11} & \mathbf{0} & \cdots & \mathbf{0} \\ \mathbf{0} & \mathbf{T}_{22} & \cdots & \mathbf{0} \\ \vdots & \vdots & \ddots & \vdots \\ \mathbf{0} & \mathbf{0} & \cdots & \mathbf{T}_{NN} \end{pmatrix}. \tag{20}$$

This filter allows to obtain the interferometric coherences as the numerical range of the $\mathbf{\Pi}_{ij}$ matrices [9], [27]

$$\mathbf{\Pi}_{ij} = \mathbf{T}_{ii}^{-\frac{1}{2}} \mathbf{\Omega}_{ij} \mathbf{T}_{jj}^{-\frac{1}{2}}. \tag{21}$$

According to the two-layer model, the polarimetric (13) and PolInSAR (14) matrices in the whitened domain are rewritten as

$$\mathbf{I} = \mathbf{T}_{gw} + \mathbf{T}_{vw} \tag{22}$$

$$\widetilde{\mathbf{\Pi}}_{ij} = \gamma_{ij}^g \mathbf{T}_{gw} + \gamma_{ij}^v \mathbf{T}_{vw} \tag{23}$$

$$\mathbf{T}_{ii} = \mathbf{T}_{ii}^{\frac{1}{2}} \left(\mathbf{T}_{gw} + \mathbf{T}_{vw} \right) \mathbf{T}_{ii}^{\frac{1}{2}} = \mathbf{T}_{g_{ii}} + \mathbf{T}_{v_{ii}} \tag{24}$$

where $\mathbf{T}_{gw}$ and $\mathbf{T}_{vw}$ are the whitened polarimetric ground and volume coherency matrices. While $\mathbf{T}_{gw}$ and $\mathbf{T}_{vw}$ are, by definition, constant across acquisitions, $\mathbf{T}_{g_{ii}}$ and $\mathbf{T}_{v_{ii}}$ may be different for each acquisition i after the dewhitening through (24)

$$\mathbf{T}_{g_{ii}} = \mathbf{T}_{ii}^{\frac{1}{2}} \mathbf{T}_{gw} \mathbf{T}_{ii}^{\frac{1}{2}} \tag{25}$$

$$\mathbf{T}_{v_{ii}} = \mathbf{T}_{ii}^{\frac{1}{2}} \mathbf{T}_{vw} \mathbf{T}_{ii}^{\frac{1}{2}}. \tag{26}$$

Note that this whitening process only affects the polarimetric information. Therefore, the whitened $\mathbf{Z}_w$ in (19) may be approximated by an SKP form with the same structure matrices as in (17)

$$\widetilde{\mathbf{Z}}_w = \mathbf{R}_g \otimes \mathbf{T}_{gw} + \mathbf{R}_v \otimes \mathbf{T}_{vw}. \tag{27}$$

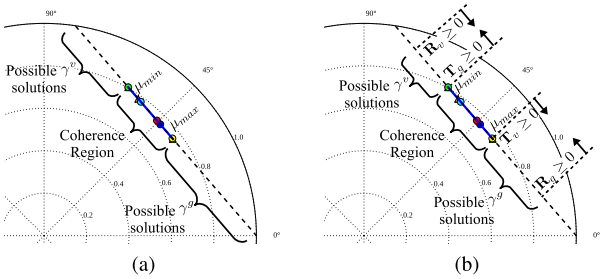

Fig. 3. Two-layer model ambiguities for γ^g and γ^v selection in (a) single-baseline and (b) multibaseline configurations.

B. Ground and Volume Polarimetric Components

From (22) and (23), the whitened ground and volume coherency matrices $\mathbf{T}_{gw}$ and $\mathbf{T}_{vw}$ are estimated from the interferometric ground and volume coherences

$$\mathbf{T}_{vw} = H\left(\frac{\mathbf{\Pi}_{ij} - \gamma^g_{ij}\mathbf{I}}{\gamma^v_{ij} - \gamma^g_{ij}}\right) \tag{28}$$

$$\mathbf{T}_{gw} = H\left(\frac{\mathbf{\Pi}_{ij} - \gamma^v_{ij}\mathbf{I}}{\gamma^g_{ij} - \gamma^v_{ij}}\right) \tag{29}$$

where $H(\mathbf{A})$ denotes the Hermitian part of matrix $\mathbf{A}$, defined as $H(\mathbf{A}) = (\mathbf{A} + \mathbf{A}^H)/2$. In the multibaseline case, the average of the ground and volume components $\mathbf{T}_{vw}$ and $\mathbf{T}_{gw}$ in (28) and (29) over all the baselines may be performed.

From these equations, one can observe that the separation of ground and volume polarimetric responses $\mathbf{T}_{g_{ii}}$ and $\mathbf{T}_{v_{ii}}$ reduces to estimating their respective interferometric coherences γ^g_{ij} and γ^v_{ij}.

C. Ground and Volume Coherence Estimation Ambiguities

As mentioned before, the observed PolInSAR coherence region represents only a segment of the line between γ^g_{ij} and γ^v_{ij}. This poses a problem for model inversion since all the points in the line outside the coherence region are possible solutions for γ^g_{ij} and γ^v_{ij} [10]. A representation of these ambiguities in the complex plane is shown in Fig. 3(a). The model inversion is ambiguous and, therefore, several equally valid $\mathbf{T}_{gw}$ and $\mathbf{T}_{vw}$ responses may be extracted.

Assuming coherence linearity, fixing one of the coherences defines the coherency matrix of the other component up to a scalar factor. This is observed in (28) and (29), where the numerators are matrices while the denominators correspond to scalars. This scalar factor is inversely proportional to the distance between ground and volume coherences. For instance, fixing the ground coherence γ^g_{ij} defines the coherency matrix of the volume $\mathbf{T}_{vw}$ up to a scalar factor $1/(\gamma^v_{ij} - \gamma^g_{ij})$. This effect is shown in Fig. 4, where the volume coherence is changed over the range of possible γ^v_{ij} solutions shown in Fig. 3(a). To illustrate this, the total power (coherency matrix trace) and polarimetry (entropy H and mean alpha angle $\bar{\alpha}$ parameters) of the extracted ground and volume components are shown. It can be seen that the power distribution of both components is changing (top plot), but only the polarimetry of the ground component varies (bottom plot). From (28), a scalar factor c of the same volume $c \cdot \mathbf{T}_{vw}$ is obtained when changing γ^v_{ij} over the line, resulting in a constant plot for H_v and $\bar{\alpha}_v$.

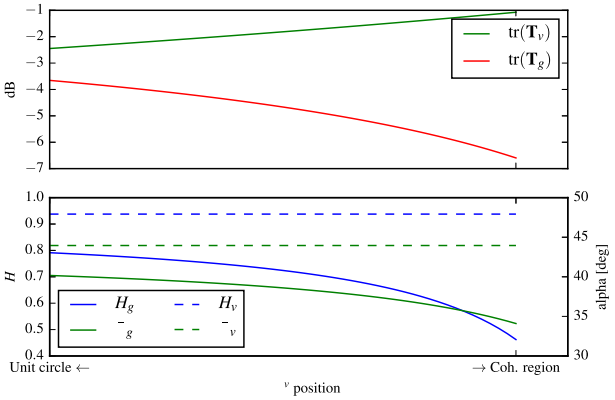

Fig. 4. Effect of the volume coherence γ^v selection over the range shown in Fig. 3(a) on the extracted ground $\mathbf{T}_g$ and volume $\mathbf{T}_v$ components.

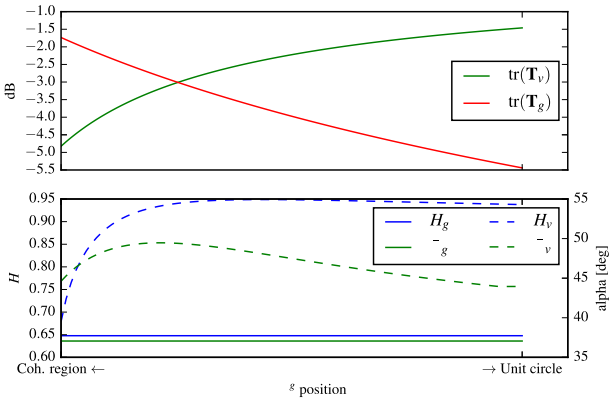

Fig. 5. Effect of the ground coherence γ^g selection over the range shown in Fig. 3(a) on the extracted ground $\mathbf{T}_g$ and volume $\mathbf{T}_v$ components.

The symmetric behavior is observed when changing the ground coherence while keeping the volume coherence fixed, as shown in Fig. 5. In this case, the polarimetry of the ground is fixed up to a scalar factor ($c \cdot \mathbf{T}_{gw}$), while the H_v and $\bar{\alpha}_v$ components change when varying γ^g_{ij}.

The ambiguity in the selection of γ^g_{ij} is usually resolved by assuming that the ground is an impenetrable surface. Thus, in the absence of nonvolumetric decorrelation sources, the ground coherence lies on the unit circle, as $|\gamma^g_{ij}| = 1$ Under this assumption, γ^g_{ij} can be estimated as the intersection of the coherence line with the unit circle [10]. To resolve the ambiguity in γ^v_{ij}, an additional assumption is required. Commonly, $\mu_{min} = 0$ is assumed [10], which corresponds to fixing γ^v_{ij} at the end of the coherence region. This suggests that there is a polarization with no ground scattering contribution, which implies that the ground coherency matrix is of rank 2. This regularization might be reasonable at higher frequencies, dense and tall vegetation but becomes problematic at lower frequencies and sparser vegetation, where a significant ground contribution can be present at all the polarizations. In those cases in which this assumption does

not hold, the obtained ground and volume components may be biased.

In the multibaseline scenario, it is worth noticing that adding more baselines does not help to resolve the ambiguities. We are adding more observations but also more unknowns, as the corresponding layer coherences γ_{ij}^{g} and γ_{ij}^{v} should also be estimated for the new baselines. However, although adding more baselines does not resolve the ambiguity, it may reduce its region length. The fact that structure matrices also need to be positive semidefinite, i.e., $\mathbf{R}_g, \mathbf{R}_v \geq 0$, imposes additional constraints on the possible coherence γ_{ij}^{l} values, as shown in the structure matrices definition in (18). These positive semidefinite constraints for coherency and structure matrices are represented in Fig. 3(b). In the single-baseline case, as only one coherence is contained in the structure matrices, the positive semidefinite constraint reduces to $|\gamma^{l}| \leq 1$.

D. Adding a Vertical Reflectivity Profile Parametrization

Another approach to solve the mentioned ambiguities and, at the same time, to extract bio/geophysical properties of the scene from PolInSAR data is to assume a vertical reflectivity profile parametrization for the ground and volume components, i.e., $F^{g}(z, \mathbf{\Phi}_g)$ and $F^{v}(z, \mathbf{\Phi}_v)$. Thus, the vertical reflectivity profiles can be characterized by a small number of parameters, represented by $\mathbf{\Phi}_g$ and $\mathbf{\Phi}_v$. Moreover, the ground and volume coherences of different baselines, $\gamma_{ij}^{g}(\mathbf{\Phi}_g)$ and $\gamma_{ij}^{v}(\mathbf{\Phi}_v)$, can now be related with these parameters through (11). Then, the model inversion process now involves the estimation of the $\mathbf{\Phi}_g$ and $\mathbf{\Phi}_v$ parameters that are possible solutions to the two-layer model, as previously discussed in Section III-C. If the number of parameters required for the profile parametrization is smaller than the number of baseline combinations, the inversion problem may be solved. This corresponds to the second assumption highlighted in Fig. 2.

As already mentioned, one common profile parametrization is to assume the ground layer as an impenetrable surface [10]. This means that the vertical reflectivity profile of the ground layer $F^{g}(z)$ corresponds to a delta function located at the ground level h_0

$$F^{g}(z, h_0) = \delta(z - h_0). \tag{30}$$

The corresponding ground coherences γ_{ij}^{g} will be at the unit circle for all the baselines, according to (11) [10]

$$\gamma_{ij}^{g}(h_0) = e^{j\phi_{ij}^{0}} = e^{jk_{z_{ij}}h_0} \tag{31}$$

where ϕ_{ij}^{0} represents the ground phase and h_0 is the ground layer height with respect to the reference.

The volume component has been traditionally described by physical models as a uniform volume extending vertically from the ground h_0 up to a given height h_v. This parametrization leads to an exponential extinction vertical profile [3], [10]

$$F^{v}(z, h_v, \sigma_v, h_0) = e^{-2\sigma_v(h_v + h_0 - z)/\cos\theta} \tag{32}$$

$$\gamma_{ij}^{v}(h_v, \sigma_v, h_0) = \frac{2\sigma e^{jk_{z_{ij}}h_0}}{\cos\theta\left(e^{2\sigma h_v/\cos\theta} - 1\right)} \cdot \int_0^{h_v} e^{jk_{z_{ij}}z} e^{2\sigma z/\cos\theta}\, dz \tag{33}$$

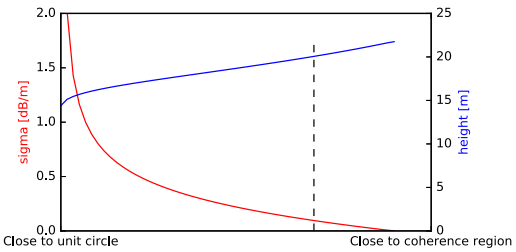

Fig. 6. Height and extinction values obtained for the possible solution of the line. The simulated values (h_v = 20 m and σ_v = 0.1 dB/m) are marked by the intersection with the vertical dotted line.

where h_v and σ_v represent the volume layer height and extinction, respectively, and θ represents the incidence angle.

While these vertical reflectivity profile approximations are standard in PolInSAR forest height inversion, deviations may occur in the presence of complex subsurface ground scattering or highly stratified vegetation structures. Nevertheless, this simplified layer parametrization has proven to be sufficiently robust to characterize the scattering contributions in a wide variety of forest scenarios, especially at lower frequencies [3], [10], effectively balancing model complexity with observation space dimensionality. In the following, the PolInSAR two-layer model ground and volume decomposition using a uniform volume parametrization with exponential extinction for the single-baseline and multibaseline cases are addressed.

1) Single-Baseline Inversion: The first step is to estimate the coherence line. Several methods may be found in the literature as, for instance, a linear regression of a set of coherence values for different polarizations [10] or a Frobenius norm minimization [26] of the full PolInSAR matrix.

Assuming the delta profile defined in (30) and (31), the ground coherence will be at the intersection of the coherence line with the unit circle, solving one of the ambiguities shown in Fig. 3(a). The volume coherence may be moved from the end of the coherence region, following the line, to the unit circle, as all the points outside the coherence region are equally valid solutions [γ^{v} ambiguity in Fig. 3(a)] [10]. The single-baseline observation space cannot resolve the remaining ambiguity in the location of the volume coherence with the model described in (32) and (33), as several combinations of height h_v and extinction σ_v parameters may lead to these γ^{v} values, as shown in Fig. 6 for the simulated data of the example in Fig. 3(a).

However, there are ways to regularize the problem and obtain an approximate estimate of γ^{v}. One possible regularization is, for example, to fix the volume extinction σ_v parameter while allowing to change the height h_v. This allows the estimation of a volume coherence located beyond the end of the visible coherence line and so the estimation of a rank 3 ground coherence matrix.

Instead of using the uniform volume, another approach to solve the ambiguity would be to fix the normalized vertical reflectivity profile shape while changing only the vertical extent of it. In this case, the volume reflectivity profile will be parametrized with just one parameter, the height h_v, and a single-baseline PolInSAR acquisition will be enough to

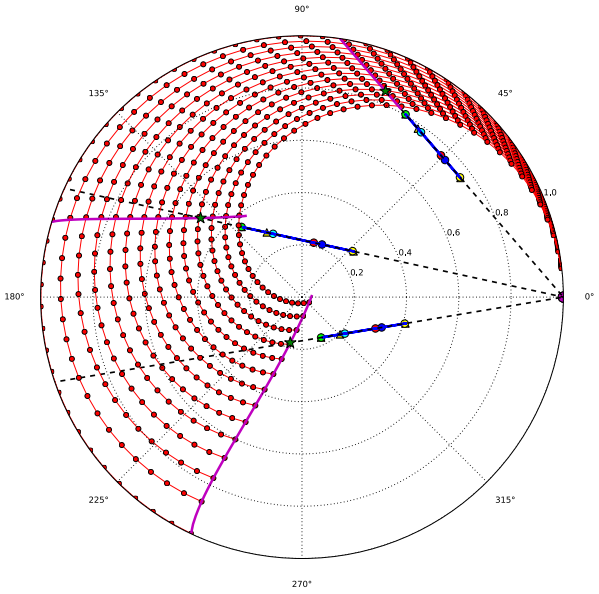

Fig. 7. Simulated coherence regions with $h_v = 20$ m and $\sigma_v = 0.1$ dB/m for $k_z = (0.1, 0.2, 0.3)$. The possible solutions for the $k_z = 0.1$ line are marked in magenta. The corresponding (h_v, σ_v) set of values of these solutions (see Fig. 6) have been projected over the other two coherence lines with $k_z = (0.2, 0.3)$. Red lines mark the volume coherences evolution for these solutions while increasing k_z in the interval $[0, 0.3]$. The magenta lines intersect the coherence lines only at the simulated γ^v, marked with a green star for each k_z.

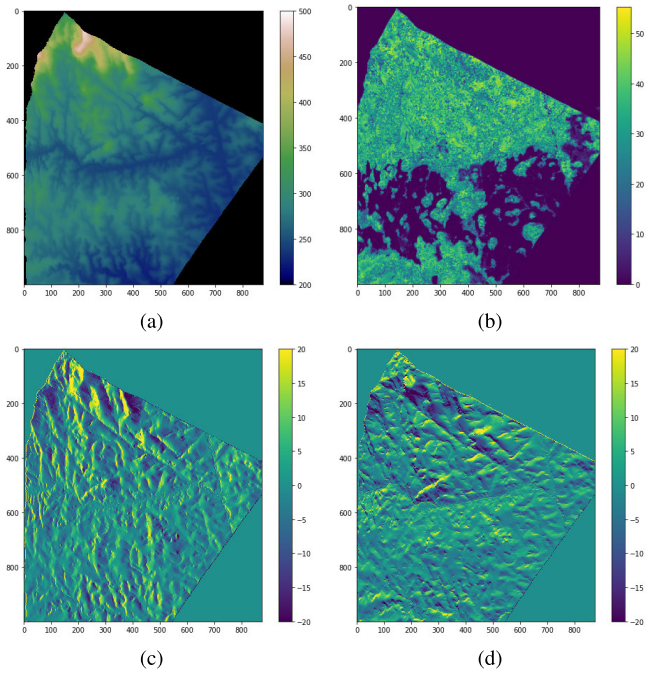

Fig. 8. Lidar (a) reference terrain model and (b) forest height. (c) Range and (d) azimuth slopes.

resolve the ambiguity, potentially extracting full-rank ground and volume components. This approach may be useful in the context of new SAR missions like ESA BIOMASS [29], [30], where the vertical reflectivity profile shape will be extracted during the first tomographic phase and can be later used during the interferometric phase [31], with a more limited number of baselines.

2) Multibaseline Inversion: In general, a unique solution may be obtained in the multibaseline case if more baselines than profile parameters are available. When N acquisitions are available, the least-square minimization may be performed over the whitened multipolarization multibaseline coherency matrix $\mathbf{T}_w$. With the exponential profile parametrization described previously, this can be expressed as

$$\min_{h_0, h_v, \sigma_v} \sum_{i,j|i<j}^{N} \left\| \mathbf{\Pi}_{ij} - \left(\gamma_{ij}^v \mathbf{T}_{vw} + \gamma_{ij}^g \mathbf{T}_{gw} \right) \right\|_F^2 \tag{34}$$

where $\mathbf{T}_{vw}$ and $\mathbf{T}_{gw}$ may be estimated as the all-baselines average of the Hermitian part of the matrices defined in (28) and (29) and the ground and volume coherences γ_{ij}^g and γ_{ij}^v are defined in (31) and (33).

In order to better understand why imposing a vertical reflectivity parametrization solves the h_v and σ_v ambiguities previously discussed in a multibaseline acquisition, Fig. 7 shows the set of solutions of Fig. 6 for the single-baseline case, the magenta lines, projected over the same simulated coherence lines for different baselines. As it may be seen, the set of parameter solutions valid for the first baseline ($k_z = 0.1$) only intersects the coherence lines from other baselines at one point, marked with a green star, corresponding to the simulated model parameters. This means that, when combining different baselines, there is only one model parameter solution that is valid for all of them at the same time, corresponding to the real value. This was already noticed in [32], where dual-baseline PolInSAR data were used to solve the uniform volume with exponential extinction model in (33).

It may also be seen in Fig. 7 that the larger the baseline difference, the larger the intersection angle between the solution space lines. This means that, in order to have good conditioning for an unambiguous model inversion, significantly different baselines should be preferred. On the other hand, larger baselines are usually affected by a stronger volume decorrelation, resulting in lower coherences, which suffer from stronger variance and larger estimation bias [33]. This suggests that there is a tradeoff between the distinct baseline values and its separation for a stable and well-conditioned model inversion. It is also worth mentioning here that the coherence separation on the complex plane is dependent on the product between the vertical wavenumber k_z and the volume height h_v, as it may be seen in (33), involving that the preferred baselines depend also on the vegetation layer height [34]. In this context, a multibaseline approach has the advantage of potentially having a good set of baselines for a wide range of scenarios.

IV. Results and Discussion

In order to demonstrate the proposed approach, experimental data acquired in the context of the AfriSAR campaign are used. The campaign was conducted in 2015 and 2016 as a joint effort of different space agencies ESA, NASA, ONERA, German Aerospace Center (DLR), and AGEOS over different forest sites in Gabon [35], [36]. In this work, L-band and

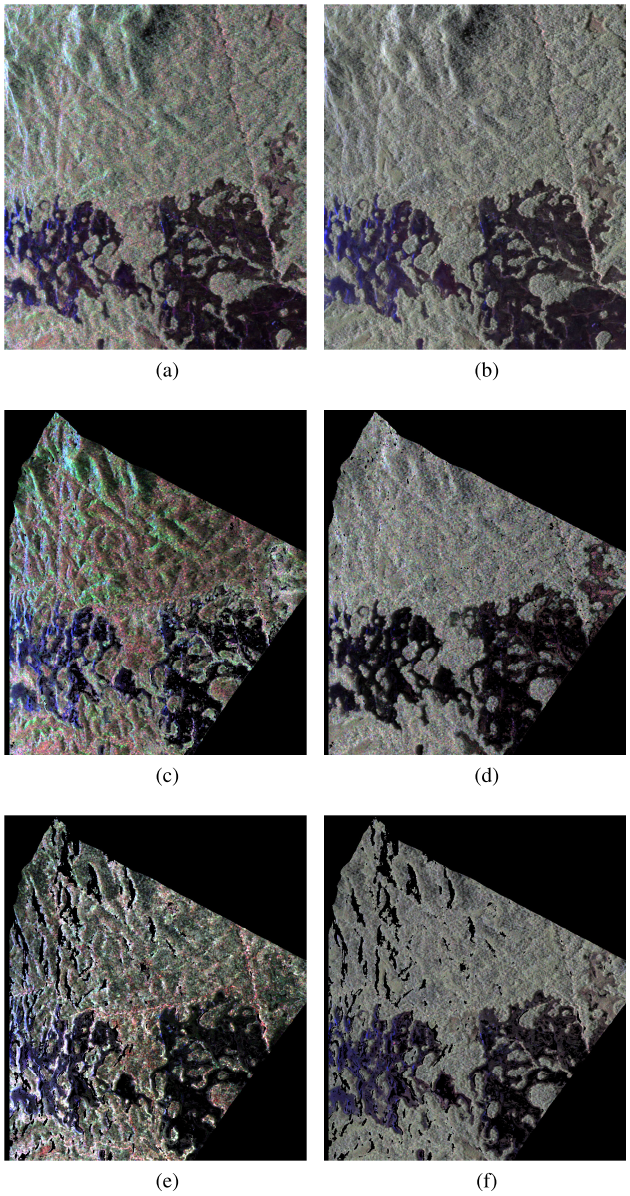

Fig. 9. Pauli RGB of the reference acquisition at (a) P-band and (b) L-band. The extracted ground and volume components with the multibaseline approach are shown in (c) and (d) and (e) and (f) for P-band and L-band, respectively. Black areas in (c)–(f) correspond to masked areas where no DTM is available or where the model could not be inverted.

P-band SAR quad-polarimetric acquisitions performed by DLR's FSAR airborne sensor are used, acquired in February 2016 in a repeat-pass interferometric mode over the Lopé site. This site is located within the Lopé National Park and features a variety of structure types ranging from open savannas to undisturbed tall (sometimes exceeding 50 m) dense forest stands [37], [38]. The terrain is hilly with local slopes steeper than 20°, as it may be seen in Fig. 8. The Pauli RGB color composite [2] of the reference (e.g., "primary") acquisition at P-band and L-band are shown in Fig. 9(a) and (b). In both frequencies, the terrain modulation of the scattering behavior is evident.

The SAR dataset consists of 12 airborne acquisitions acquired on February 10, 2016. L-band and P-band were simultaneously acquired at different vertical baselines with respect to the reference at approximately +10, ±20, ±40, ±60, and ±80 m and two additional horizontal baselines at +5 and +10 m, allowing vertical wavenumbers with respect to the reference at the center of the scene ranging approximately from −0.17 to 0.17 rad/m at P-band and from −0.5 to 0.5 rad/m at L-band. Additionally and almost parallel to the SAR measurement campaign, a high-resolution lidar dataset has been acquired, covering part of the Lopé test site. From this lidar, the DTM and forest height have been extracted, as shown in Fig. 8(a) and (b) in radar geometry. The range and azimuth slopes may be obtained from the DTM, as shown in Fig. 8(c) and (d), respectively. As it may be seen, large topographic features may be observed on the Lopé test site with several hilly slopes.

It is worth noting that while the lidar data enables the quantitative validation of the geometric estimates, no ground truth is available to directly validate the separated polarimetric responses of the ground and volume layers. Consequently, the performance of the polarimetric decomposition is evaluated based on the physical consistency of the results and their correlation with the expected terrain features.

A. Multibaseline Results

First, the multibaseline approach, as defined in Section III-D2, is analyzed and discussed, as it allows to remove the mentioned model inversion ambiguities assuming an exponential vertical reflectivity model. Afterward, the single-baseline approach will be considered. Although in theory only two different baselines are required in order to solve the ambiguity, here for completeness all the baselines are used, and the minimization in (34) is performed, using the ground delta and volume exponential vertical reflectivity models defined in (31) and (33). The Pauli RGB of the reference images at P-band and L-band may be seen in Fig. 9(a) and (b), respectively. Similarly, the Pauli RGB of the obtained coherency matrices $\mathbf{T}_{g_{11}}$ and $\mathbf{T}_{v_{11}}$ for the ground and volume components of the same image are represented in Fig. 9(c) and (d) and (e) and (f), respectively. The areas where the model could not be inverted are represented in black. They are mainly surface and bare areas, where the two-layer model does not apply. The lidar DTM shown in Fig. 8(a) has been employed to fix the ground level, as it will be used in the following to analyze the obtained components. For this reason, the areas where no lidar information is available have also been masked in Fig. 9(c)–(f).

As it may be seen in Fig. 9, the obtained volume components, in Fig. 9(d) and (f), are very homogeneous, presenting only some small intensity variations. On the other hand, the ground component, shown in Fig. 9(c) and (e), presents a larger variability, presenting many more details of the image. This is especially clear looking at the variations induced by topography, which appear clearly on the ground component but they are almost not visible on the volume. Moreover, the ground component presents a larger variability in terms of the type of scattering, as it may be seen in the color variation in Fig. 9(c) and (e) with respect to Fig. 9(d) and (f).

In order to complement the Pauli RGB images, Fig. 10 shows the entropy (H), anisotropy (A), and mean alpha angle

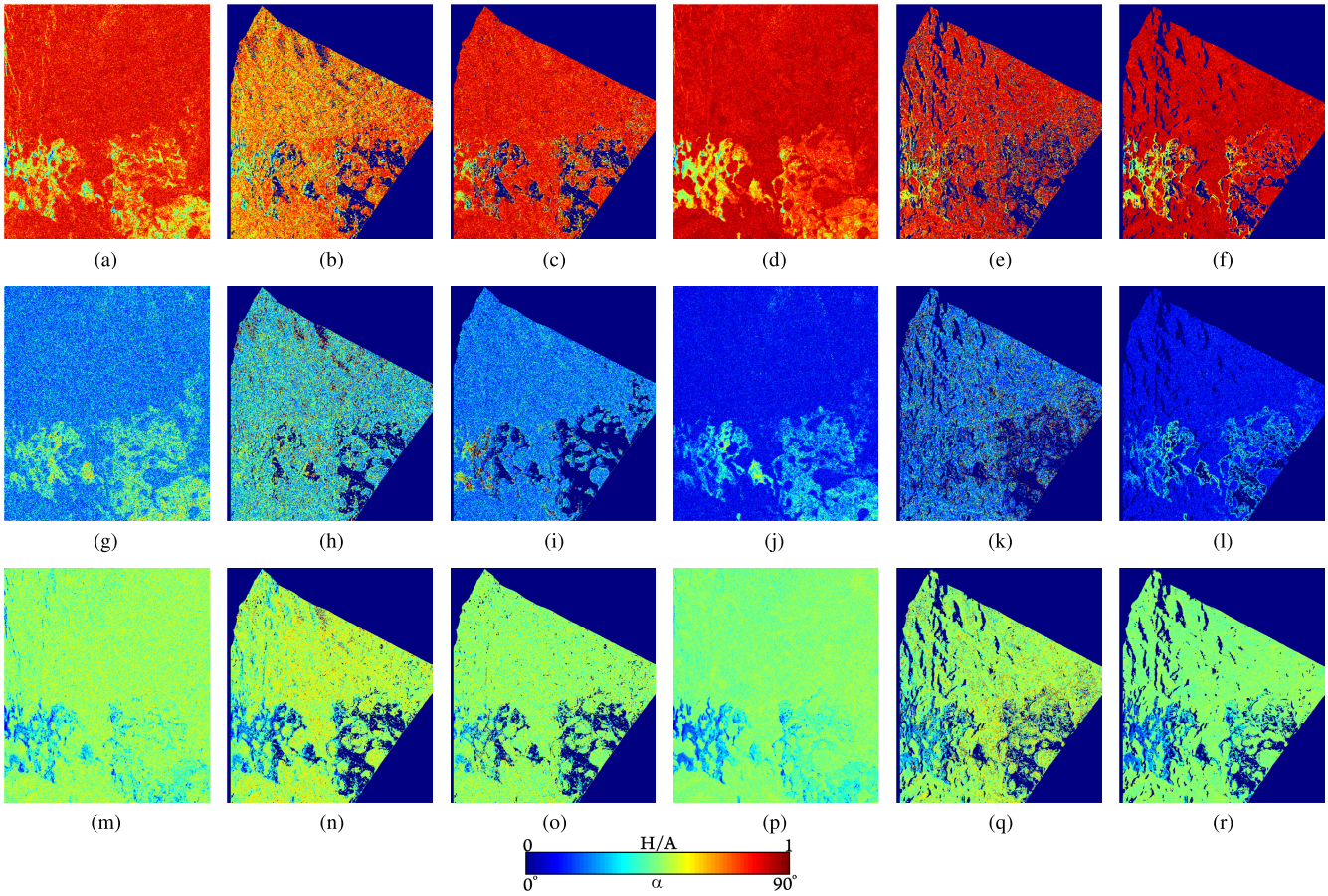

Fig. 10. Entropy (H), anisotropy (A), and mean alpha angle ($\bar{\alpha}$), in rows, of the reference acquisition, ground, and volume components at P-band and L-band, in columns. (a) H original P-band. (b) H ground P-band. (c) H volume P-band. (d) H original L-band. (e) H ground L-band. (f) H volume L-band. (g) A original P-band. (h) A ground P-band. (i) A volume P-band. (j) A original L-band. (k) A ground L-band. (l) A volume L-band. (m) $\bar{\alpha}$ original P-band. (n) $\bar{\alpha}$ ground P-band. (o) $\bar{\alpha}$ volume P-band. (p) $\bar{\alpha}$ original L-band. (q) $\bar{\alpha}$ ground L-band. (r) $\bar{\alpha}$ volume L-band.

($\bar{\alpha}$) parameters of the Cloude–Pottier decomposition [4] for the original, ground, and volume components at P-band and L-band. All the decomposition parameters (H, A, and $\bar{\alpha}$) present more homogeneous values for the volume than for the ground component. In addition, it may be seen that the volume component is characterized by a large entropy (H), low anisotropy (A), and a mean alpha angle close to 45°, corresponding to a random volume according to traditional scattering models. The ground component, on the other hand, has a larger variability, covering a wider range of values for the decomposition parameters.

Fig. 11 shows the span (i.e., the matrix trace) of the original, ground, and volume components (defined as $\mathrm{tr}(\mathbf{T}_{g_{11}})$ and $\mathrm{tr}(\mathbf{T}_{v_{11}})$, respectively) as a function of the terrain range slope, only for forested areas in the scene. They have been selected by thresholding the lidar-derived forest heights at 10 m. The top row [see Fig. 11(a)–(c)] shows the P-band, while the bottom row [see Fig. 11(d)–(f)] corresponds to the L-band plots. At P-band, the slope dependency of the volume component (see Fig. 11) is slightly reduced when compared with the original data [see Fig. 11(a)]. This is caused by the ground scattering contribution included in the original data. This effect is smaller at L-band, due to the lower ground scattering contribution in the original data, which becomes clear comparing Fig. 11(c) with Fig. 11. As it may be seen, the

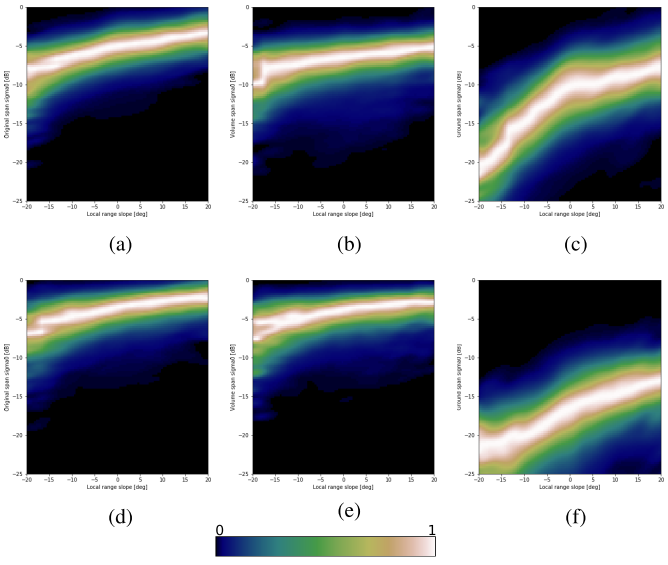

Fig. 11. Span of the original, volume, and ground components, respectively, with respect to local slopes at (a)–(c) P-band and (d)–(f) L-band.

dependency on the slope is larger for the ground component [see Fig. 11(c) and (f)], appearing as a more tilted curve for both P-band and L-band. In Fig. 11(c), it may also be seen

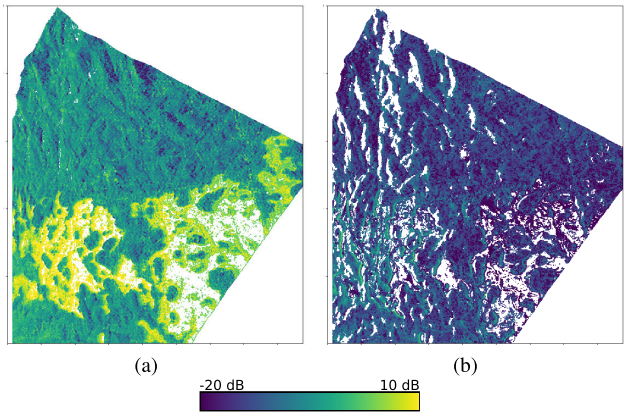

Fig. 12. Span ground to volume ratio at (a) P-band and (b) L-band.

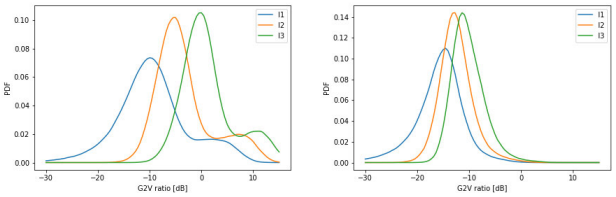

Fig. 13. Distributions of the ground to volume ratio generalized eigenvalues at (a) P-band and (b) L-band.

a small increase of the ground at P-band around 0° slopes, corresponding to the dihedral ground–trunk component that is relevant when they are perpendicular.

In order to see in more detail the difference between P-band and L-band in terms of components power distribution, Fig. 12 shows the span ground to volume ratio, defined as $\mathrm{tr}(\mathbf{T}_{g_{11}})/\mathrm{tr}(\mathbf{T}_{v_{11}})$, over the scene. In general, the ground-to-volume ratio observed at L-band is around 10 dB smaller than at P-band. This difference is mostly produced by the decrease of the ground power due to the larger attenuation of the forest canopy at L-band. The plots shown on Fig. 11(c) and (f) confirm this. Moreover, there is a small increase of the volume component at L-band with respect to P-band, as seen on Fig. 11(b) and (e), that also contributes to this difference in the ground to volume ratio. Similarly, the effects of the local topography on the ground to volume ratio appear also clear in Fig. 12.

However, Fig. 12 only shows the ratio of the total ground and volume powers, but the ground-to-volume ratio changes with polarization, as described before. Fig. 13 shows the distribution of the eigenvalues of the ground to volume matrix $\mathbf{M} = \mathbf{T}_{v_{11}}^{-1}\mathbf{T}_{g_{11}}$, which maximize and minimize $\mu(\mathbf{w})$ in (12) [39], [40], over the image. Apart from the difference in the mean values previously discussed, it may also be seen that the difference between the maximum and minimum ground-to-volume ratios (μ_{max} and μ_{min}), corresponding to the difference between λ_1 and λ_3, is larger at P-band than at L-band. This implies that a bigger portion of the coherence line will be visible at P-band, making the model inversion easier and more robust. It should be noted that these results apply to tropical forests, according to the dataset employed, where the canopy density is high.

Several scattering contributions may be found at the ground level, i.e., surface, ground–trunk, and ground–volume interactions. Among them, the surface scattering is particularly interesting as it has a characteristic polarimetric signature that may be identified through the topographic features of the image. Particularly, the polarimetric orientation angle (POA) is the rotation of the polarimetric response due to the rotation of the scattering plane [41]. The orientation angle shift depends on the incidence angle θ and on the range and azimuth slope, ϕ_r and ϕ_a, respectively. This information may be extracted from the reference lidar DTM, shown in Fig. 8. The POA ψ may be then computed as [41]

$$\tan\psi = \frac{\tan\phi_a}{-\tan\phi_r\cos\theta + \sin\theta}. \tag{35}$$

Different techniques are discussed and analyzed in [41] in order to estimate the POA from the polarimetric response. From all of them, the $S_{RR}S_{LL}$ coherence seems to offer the most accurate results. Accordingly, the POA estimated $\hat{\psi}$ from SAR data may be obtained as

$$\hat{\psi} = \left(\arg\left(< S_{RR}S_{LL}^{*} >\right) + \pi\right)/4 \tag{36}$$

and replacing afterward the values where $\hat{\psi} > \pi/4$ by $\hat{\psi} - \pi/2$ [41].

Fig. 14(a) shows the POA ψ estimated from the lidar DTM, whereas Fig. 14(b)–(g) shows the POA $\hat{\psi}$ estimated using (36) on the original [see Fig. 14(b) and (c)], decomposed volume [see Fig. 14(d) and (e)], and ground [see Fig. 14(f) and (g)] components at P-band (left column) and L-band (right column). Some correlation may be found between the DEM-derived ψ and the ones estimated $\hat{\psi}$ from the original data, although the results are quite noisy due to the presence of the volume layer. On the ground component, shown in Fig. 14(f) and (g), the obtained $\hat{\psi}$ is more similar to the expected POA, especially at P-band. At L-band, the results are not so close to ψ as, due to the shorter wavelength, the surface scattering becomes more rough and less related to the orientation. In addition, the smaller ground-to-volume ratio at L-band (see Fig. 12) makes the estimation of the ground component more difficult. The estimated POA $\hat{\psi}$ from the volume component is completely noisy in both frequencies, as it may be seen in Fig. 14(d) and (e), as it is unrelated to the orientation of the azimuth slopes. The pdf of the POA estimation error $(\hat{\psi} - \psi)$ is shown in Fig. 15(a) and (b) for P-band and L-band for the original, volume and ground components. These plots show clearly the larger dependency of the ground component to the POA due to a larger surface component present, especially at P-band.

B. Single-Baseline Results

For the single-baseline case, as discussed in Section III-D1, the model inversion is, in general, ambiguous. There are, however, ways to constrain the solution space and obtain unique solutions by introducing some regularization. Here, the volume coherence has been fixed at the end of the coherence region (i.e., to assume that there is one polarization with no

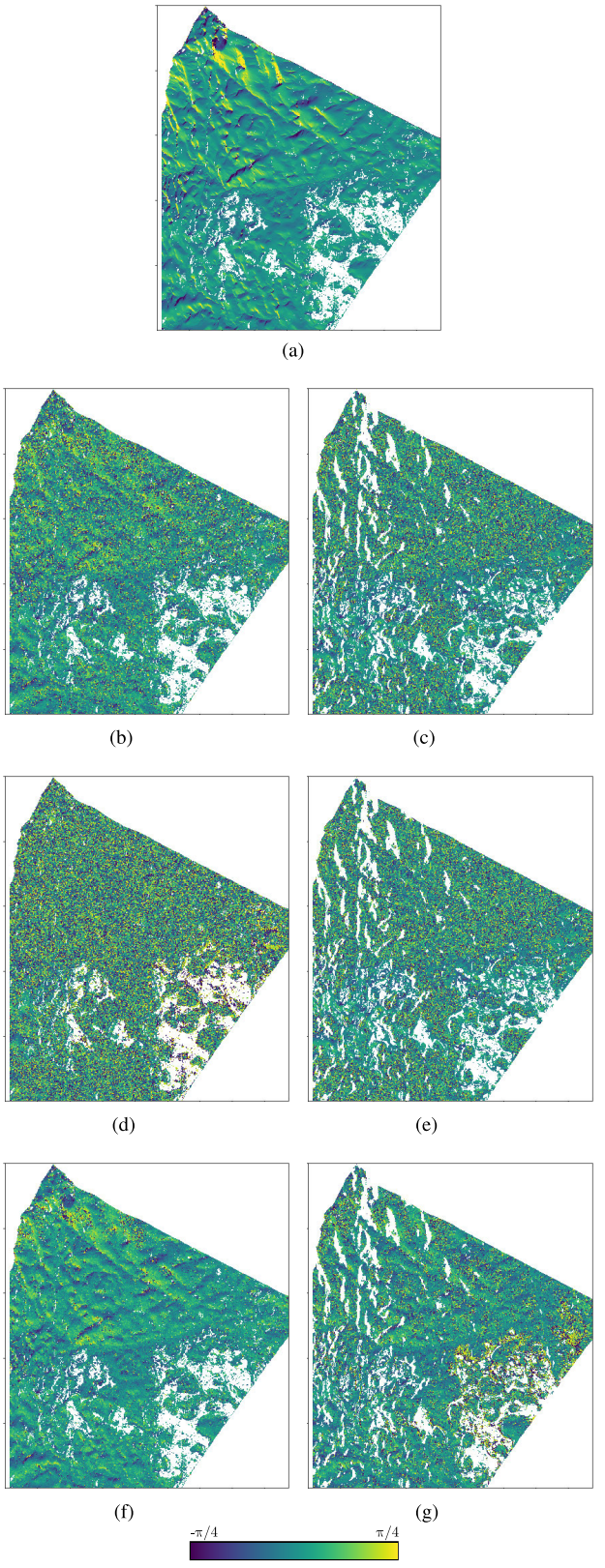

Fig. 14. POA obtained from lidar DTM and estimated from original data and ground and volume components at P-band and L-band. (a) ψ from DTM. (b) $\hat{\psi}$ original P-band. (c) $\hat{\psi}$ original L-band. (d) $\hat{\psi}$ volume P-band. (e) $\hat{\psi}$ volume L-band. (f) $\hat{\psi}$ ground P-band. (g) $\hat{\psi}$ ground L-band.

ground scattering contribution), resulting in a rank 2 coherency matrix for the ground component, as explained before. Fig. 16

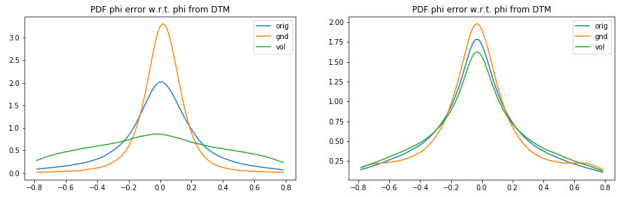

(a) (b)

Fig. 15. Distributions of the estimated POA error at (a) $\hat{\psi} - \psi$ P-band and (b) $\hat{\psi} - \psi$ L-band.

shows the Pauli RGB of the obtained ground and volume components at P-band for six different baselines. As it may be seen, very similar results are obtained for all the baselines, especially for the volume component.

To compare with the previous multibaseline analysis, the POA is estimated from the reconstructed ground and volume scattering contributions and compared with the POA estimated from the DTM. The histograms of the difference between the two POAs for different baselines are shown in Fig. 17. In all cases, the obtained behavior between the ground and volume components is different, obtaining a much flatter pdf for the volume, as expected, while the ground component concentrates around 0. However, some baseline dependency may also be observed, as too small or too large baselines, as Fig. 17(a) or (e), present lower peaks around 0 for the ground component. This may be caused by the lack of vertical sensitivity in the lower baselines and due to the increased noise and bias due to lower coherences in large baselines where more volume decorrelation may occur [34]. Comparing the multibaseline with the single-baseline decomposition results makes clear that the multibaseline approach performs better by means of providing a rank 3 ground scattering component and a POA that fits better to the one derived from the DTM, as the $\hat{\psi} - \psi$ peak is higher for the ground component.

C. Comparison With Existing Methods

In order to contextualize the obtained results, it is worth comparing the proposed methodology with other existing techniques. While other methods can extract similar information regarding the vertical structure of the scene, the proposed technique is specifically formulated to provide a complete and exact polarimetric decomposition, avoiding approximation residuals that might alter the physical signatures of the ground and volume components.

One of these relevant techniques is polarimetric SAR tomography (PolTomoSAR) [42]. PolTomoSAR provides a continuous, fully polarimetric vertical profile. However, its vertical resolution is highly dependent on the tomographic point spread function (PSF) [43]. As the number of baselines is reduced, the PSF widens, representing the spread of the reflected power over a larger vertical span. This makes the discrete extraction of ground and volume matrices less precise, especially when there is a significant power difference between the layers. On the other hand, the proposed technique explicitly assumes a Dirac delta at the ground and a vertically distributed

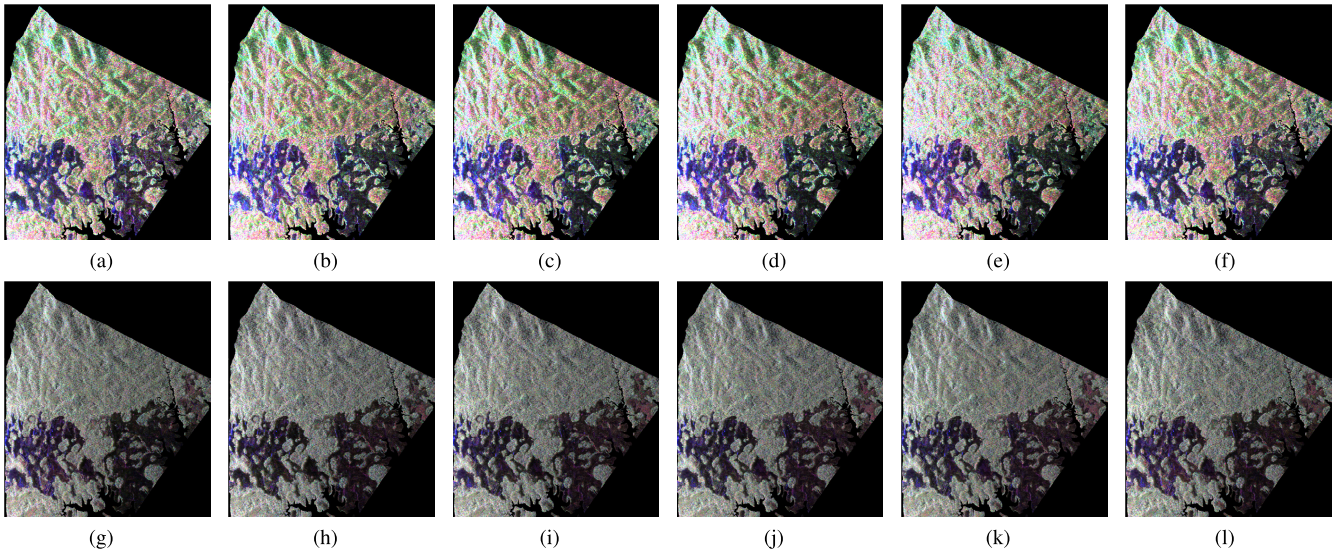

Fig. 16. Pauli RGB of the obtained ground and volume components at P-band with the single-baseline approach for different vertical baselines. (a) $\mathbf{T}_{g_{11}}$, +10 m. (b) $\mathbf{T}_{g_{11}}$, +20 m. (c) $\mathbf{T}_{g_{11}}$, +40 m. (d) $\mathbf{T}_{g_{11}}$, +60 m. (e) $\mathbf{T}_{g_{11}}$, +80 m. (f) $\mathbf{T}_{g_{11}}$, −20 m. (g) $\mathbf{T}_{v_{11}}$, +10 m. (h) $\mathbf{T}_{v_{11}}$, +20 m. (i) $\mathbf{T}_{v_{11}}$, +40 m. (j) $\mathbf{T}_{v_{11}}$, +60 m. (k) $\mathbf{T}_{v_{11}}$, +80 m. (l) $\mathbf{T}_{v_{11}}$, −20 m.

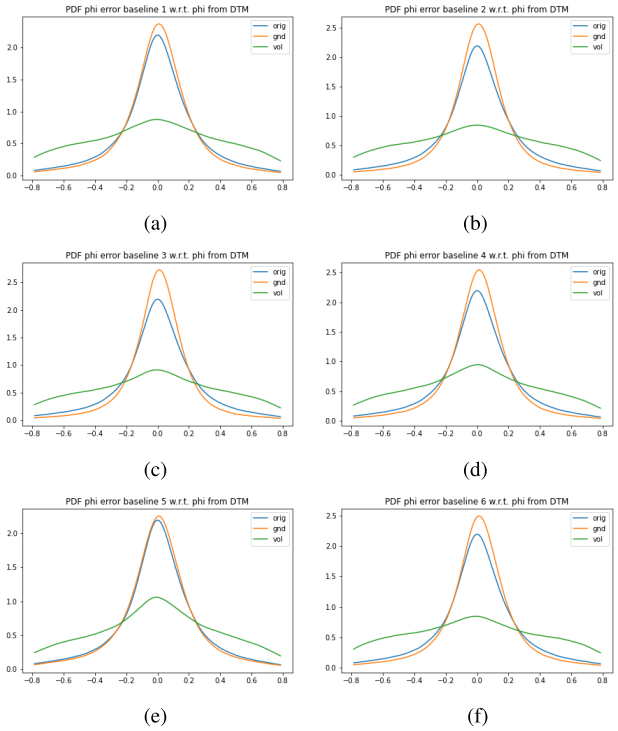

Fig. 17. Distribution of the estimated POA error from original and single baseline separated components at P-band for different baselines. (a) $\hat{\psi} - \psi$, +10 m. (b) $\hat{\psi} - \psi$, +20 m. (c) $\hat{\psi} - \psi$, +40 m. (d) $\hat{\psi} - \psi$, +60 m. (e) $\hat{\psi} - \psi$, +80 m. (f) $\hat{\psi} - \psi$, −20 m.

volume. This structural assumption overcomes the vertical resolution limitations of tomography, allowing the technique to be applied even to single-baseline data, as shown in Section IV-B.

Another relevant approach is the SKP decomposition [15], which also assumes a two-layer model. However, the SKP decomposition is based on a truncated Kronecker product singular value decomposition (KPSVD), estimating an approximated matrix $\widetilde{\mathbf{Z}}_N = \mathbf{R}_g \otimes \mathbf{T}_g + \mathbf{R}_v \otimes \mathbf{T}_v$ by minimizing the Frobenius norm error with respect to the observed matrix ($\|\mathbf{Z}_N - \widetilde{\mathbf{Z}}_N\|_F$). Our analysis over the processed dataset shows that, while the relative error of the SKP approximation over the individual PolSAR acquisitions is mostly concentrated between 5% and 15% (in line with findings in [15]), this error can easily become significantly larger than the ground component itself, frequently exceeding 100% relative error with respect to $\mathbf{T}_g$.

Therefore, while algebraic approximations like the SKP decomposition are appropriate for the extraction and analysis of vertical structural properties [16], [21], the approximation error may mask the real polarimetric signature of the smaller scattering components. In contrast, the proposed technique does not approximate the individual PolSAR acquisitions. Instead, it enforces the aforementioned exact separation for all the PolSAR matrices ($\mathbf{T}_{ii} = \mathbf{T}_{g_{ii}} + \mathbf{T}_{v_{ii}}$), concentrating the modeling error purely in the PolInSAR matrices ($\mathbf{\Pi}_{ij}$). This makes the proposed method more suitable for a precise polarimetric analysis of the separated layers.

V. Conclusion

This article proposes and discusses a new polarimetric model-based ground and volume decomposition approach for PolInSAR measurements. Under the assumption of a two-layer scattering structure, where each layer has the same vertical reflectivity profile for all polarizations, the polarimetric coherency (or covariance) matrices of the two layers can be separated without any additional constraints. This is achieved by establishing a link between the polarimetric coherency matrices of the two components and the interferometric coherences of the two layers. It is worth mentioning here that no assumptions are required with respect to the ground and volume polarimetry, as opposite to classical polarimetric decomposition techniques, having the possibility to retrieve

the full-rank coherency matrices of each layer. In addition, it is formulated as a complete decomposition where the original coherency matrix is exactly decomposed into the sum of these two layers, unlike some techniques in the literature where an approximation is obtained.

The proposed two-layer decomposition technique has been evaluated for the specific case of a vegetation layer over ground. In the forest case, the ground layer is assumed to be impenetrable with a Dirac-like vertical reflectivity response, while the second layer is a random volume. The polarimetric ground and volume coherency matrices are then directly related to the interferometric coherences of the ground and volume components. In this regard, the polarimetric decomposition problem is reduced to an interferometric coherence estimation problem.

In general, the estimation of the ground and volume interferometric coherences is ambiguous in the context of a single baseline. Even when assuming a nondecorrelating ground scattering component, there are many possible solutions for the interferometric coherence of the volume component. In this case, two ways to obtain a unique solution are proposed. The first one is to assume a 2-D ground scattering component that constrains the interferometric coherence of the volume component at the end of the coherence region, but leads to rank two ground coherence matrices. The second approach is to assume a given vertical reflectivity profile shape for the volume component and use one parameter to characterize the height, which would allow to derive rank three ground and volume coherency matrices. Despite these ambiguities, it is worth noting that, for instance, the knowledge of the interferometric ground coherence already determines the volume coherency matrix up to a scalar factor and vice versa.

When two or more PolInSAR baselines are available, a unique solution for the ground and volume coherences may be obtained, since a parametric reconstruction of the vertical reflectivity profile is possible using, for instance, an exponential profile.

Furthermore, in the presence of temporal decorrelation between acquisitions, the same technique could be applied, provided that the two-layer coherences can be properly estimated in the presence of temporal decorrelation, as some models have suggested [44], [45].

The proposed technique has been applied and evaluated with P-band and L-band PolInSAR data from the AfriSAR F-SAR campaign acquired over tropical forest on the Lopé test site. Since a direct validation is almost impossible due to the lack of reference measurements for each or even one of the layers, an indirect validation has been proposed based on the estimation of the POA from the underlying ground and its comparison with the POA derived from the lidar DTM. This indirect validation has shown very good agreement, especially at P-band, where a good correspondence between estimated and lidar-derived POA has been achieved. Results at L-band, on the other hand, do not present as good agreement, but this is a consequence of the high polarimetric entropy of the ground scattering component rather than an indicator of an insufficient decomposition performance. In both cases, better results are obtained for the multibaseline case, allowing full-rank ground and volume covariance matrices.

These results indicate that the proposed approach could allow the independent monitoring of the different layers in vegetated scenarios affected by distinct physical processes, which is relevant in view of the upcoming space-based SAR missions with a strong focus on PolInSAR and tomography, such as ESA BIOMASS.

REFERENCES

[1] A. Kostinski and W. Boerner, "On foundations of radar polarimetry," *IEEE Trans. Antennas Propag.*, vol. AP-34, no. 12, pp. 1395–1404, Dec. 1986.

[2] J.-S. Lee and E. Pottier, *Polarimetric Radar Imaging: From Basics to Applications*. Boca Raton, FL, USA: CRC Press, 2017.

[3] S. Cloude, *Polarisation: Applications in Remote Sensing*. London, U.K.: Oxford Univ. Press, 2010.

[4] S. R. Cloude and E. Pottier, "A review of target decomposition theorems in radar polarimetry," *IEEE Trans. Geosci. Remote Sens.*, vol. 34, no. 2, pp. 498–518, Mar. 1996.

[5] A. Freeman and S. L. Durden, "Three-component scattering model to describe polarimetric SAR data," *Proc. SPIE*, vol. 1748, pp. 213–224, Feb. 1993, doi: 10.1117/12.140618.

[6] A. Freeman and S. L. Durden, "A three-component scattering model for polarimetric SAR data," *IEEE Trans. Geosci. Remote Sens.*, vol. 36, no. 3, pp. 963–973, May 1998.

[7] Y. Yamaguchi, T. Moriyama, M. Ishido, and H. Yamada, "Four-component scattering model for polarimetric SAR image decomposition," *IEEE Trans. Geosci. Remote Sens.*, vol. 43, no. 8, pp. 1699–1706, Aug. 2005.

[8] Y. Yamaguchi, A. Sato, W.-M. Boerner, R. Sato, and H. Yamada, "Four-component scattering power decomposition with rotation of coherency matrix," *IEEE Trans. Geosci. Remote Sens.*, vol. 49, no. 6, pp. 2251–2258, Jun. 2011.

[9] S. R. Cloude and K. P. Papathanassiou, "Polarimetric SAR interferometry," *IEEE Trans. Geosci. Remote Sens.*, vol. 36, no. 5, pp. 1551–1565, Sep. 1998.

[10] S. R. Cloude and K. P. Papathanassiou, "Three-stage inversion process for polarimetric SAR interferometry," *IEE Proc. Radar, Sonar Navigat.*, vol. 150, no. 3, pp. 125–134, Jun. 2003.

[11] J. I. H. Askne, P. B. G. Dammert, L. M. H. Ulander, and G. Smith, "C-band repeat-pass interferometric SAR observations of the forest," *IEEE Trans. Geosci. Remote Sens.*, vol. 35, no. 1, pp. 25–35, Jan. 1997.

[12] S. R. Cloude and M. L. Williams, "The negative alpha filter: A new processing technique for polarimetric SAR interferometry," *IEEE Geosci. Remote Sens. Lett.*, vol. 2, no. 2, pp. 187–191, Apr. 2005.

[13] J. D. Ballester-Berman and J. M. Lopez-Sanchez, "Applying the freeman–durden decomposition concept to polarimetric SAR interferometry," *IEEE Trans. Geosci. Remote Sens.*, vol. 48, no. 1, pp. 466–479, Jan. 2010.

[14] Y. Cui, Y. Yamaguchi, H. Yamada, and J. Yang, "Target decomposition in polarimetric interferometric SAR," in *Proc. IEEE Int. Geosci. Remote Sens. Symp. (IGARSS)*, Jul. 2017, pp. 5282–5283.

[15] S. Tebaldini, "Algebraic synthesis of forest scenarios from multibaseline PolInSAR data," *IEEE Trans. Geosci. Remote Sens.*, vol. 47, no. 12, pp. 4132–4142, Dec. 2009.

[16] S. Tebaldini, "Single and multipolarimetric SAR tomography of forested areas: A parametric approach," *IEEE Trans. Geosci. Remote Sens.*, vol. 48, no. 5, pp. 2375–2387, May 2010.

[17] C. F. Van Loan and N. Pitsianis, "Approximation with Kronecker products," in *Linear Algebra for Large Scale and Real-Time Applications*. Cham, Switzerland: Springer, 1993, pp. 293–314.

[18] M. Pardini and K. Papathanassiou, "On the estimation of ground and volume polarimetric covariances in forest scenarios with SAR tomography," *IEEE Geosci. Remote Sens. Lett.*, vol. 14, no. 10, pp. 1860–1864, Oct. 2017.

[19] C. Lopez-Martinez and K. P. Papathanassiou, "Cancellation of scattering mechanisms in PolInSAR: Application to underlying topography estimation," *IEEE Trans. Geosci. Remote Sens.*, vol. 51, no. 2, pp. 953–965, Feb. 2013.

[20] M. Mariotti d'Alessandro, S. Tebaldini, S. Quegan, M. J. Soja, L. M. H. Ulander, and K. Scipal, "Interferometric ground cancellation for above ground biomass estimation," *IEEE Trans. Geosci. Remote Sens.*, vol. 58, no. 9, pp. 6410–6419, Sep. 2020.

[21] G. Zeng et al., "Separation of ground and volume scattering in multi-baseline polarimetric SAR data and its application in DTM and CHM inversion," *IEEE Trans. Geosci. Remote Sens.*, vol. 62, 2024. [Online]. Available: https://ieeexplore.ieee.org/document/10602543

[22] C. A. Balanis, *Advanced Engineering Electromagnetics*. Hoboken, NJ, USA: Wiley, 1999.

[23] J. Goodman, "Some fundamental properties of speckle," *J. Opt. Soc. Amer.*, vol. 66, no. 11, pp. 1145–1150, 1976.

[24] H. A. Zebker and J. Villasenor, "Decorrelation in interferometric radar echoes," *IEEE Trans. Geosci. Remote Sens.*, vol. 30, no. 5, pp. 950–959, Sep. 1992.

[25] G. Krieger et al., "TanDEM-X: A satellite formation for high-resolution SAR interferometry," *IEEE Trans. Geosci. Remote Sens.*, vol. 45, no. 11, pp. 3317–3341, Nov. 2007.

[26] Y. Cui, Y. Yamaguchi, H. Yamada, and S.-E. Park, "PolInSAR coherence region modeling and inversion: The best normal matrix approximation solution," *IEEE Trans. Geosci. Remote Sens.*, vol. 53, no. 2, pp. 1048–1060, Feb. 2015.

[27] C. López-Martínez and A. Alonso-González, "Assessment and estimation of the RVoG model in polarimetric SAR interferometry," *IEEE Trans. Geosci. Remote Sens.*, vol. 52, no. 6, pp. 3091–3106, Jun. 2014.

[28] T. Flynn, M. Tabb, and R. Carande, "Coherence region shape extraction for vegetation parameter estimation in polarimetric SAR interferometry," in *Proc. IEEE Int. Geosci. Remote Sens. Symp.*, vol. 5, Jun. 2002, pp. 2596–2598.

[29] T. L. Toan et al., "The BIOMASS mission: Mapping global forest biomass to better understand the terrestrial carbon cycle," *Remote Sens. Environ.*, vol. 115, no. 11, pp. 2850–2860, 2011. [Online]. Available: http://www.sciencedirect.com/science/article/pii/S0034425711001362

[30] S. Quegan et al., "The European space agency BIOMASS mission: Measuring forest above-ground biomass from space," *Remote Sens. Environ.*, vol. 227, pp. 44–60, Jun. 2019. [Online]. Available: https://www.sciencedirect.com/science/article/pii/S0034425719301233

[31] M. Sedehi et al., "Biomass—A fully polarimetric P-band SAR ESA mission," in *Proc. EUSAR 13th Eur. Conf. Synth. Aperture Radar*, Mar. 2021, pp. 1–5.

[32] S. R. Cloude, "Robust parameter estimation using dual baseline polarimetric SAR interferometry," in *Proc. IEEE Int. Geosci. Remote Sens. Symp.*, vol. 2, Jun. 2002, pp. 838–840.

[33] R. Touzi, A. Lopes, J. Bruniquel, and P. W. Vachon, "Coherence estimation for SAR imagery," *IEEE Trans. Geosci. Remote Sens.*, vol. 37, no. 1, pp. 135–149, Jan. 1999.

[34] F. Kugler, S.-K. Lee, I. Hajnsek, and K. P. Papathanassiou, "Forest height estimation by means of pol-InSAR data inversion: The role of the vertical wavenumber," *IEEE Trans. Geosci. Remote Sens.*, vol. 53, no. 10, pp. 5294–5311, Oct. 2015.

[35] I. Hajnsek et al., "Technical assistance for the development of airborne SAR and geophysical measurements during the AfriSAR campaign," Eur. Space Agency, Paris, France, Final Tech. Rep. 4000114293/15/NL/CT, 2011.

[36] T. Fatoyinbo et al., "The NASA AfriSAR campaign: Airborne SAR and LiDAR measurements of tropical forest structure and biomass in support of current and future space missions," *Remote Sens. Environ.*, vol. 264, Oct. 2021, Art. no. 112533.

[37] N. Labrière et al., "In situ reference datasets from the TropiSAR and AfriSAR campaigns in support of upcoming spaceborne biomass missions," *IEEE J. Sel. Topics Appl. Earth Observ. Remote Sens.*, vol. 11, no. 10, pp. 3617–3627, Oct. 2018.

[38] S. M. Marselis, H. Tang, J. D. Armston, K. Calders, N. Labrière, and R. Dubayah, "Distinguishing vegetation types with airborne waveform LiDAR data in a tropical forest-savanna mosaic: A case study in Lopé National Park, Gabon," *Remote Sens. Environ.*, vol. 216, pp. 626–634, Oct. 2018.

[39] A. Kostinski and W. Boerner, "On the polarimetric contrast optimization," *IEEE Trans. Antennas Propag.*, vol. AP-35, no. 8, pp. 988–991, Aug. 1987.

[40] A. Alonso-González, C. López-Martínez, K. P. Papathanassiou, and I. Hajnsek, "Polarimetric SAR time series change analysis over agricultural areas," *IEEE Trans. Geosci. Remote Sens.*, vol. 58, no. 10, pp. 7317–7330, Oct. 2020.

[41] J.-S. Lee, D. L. Schuler, and T. L. Ainsworth, "Polarimetric SAR data compensation for terrain azimuth slope variation," *IEEE Trans. Geosci. Remote Sens.*, vol. 38, no. 5, pp. 2153–2163, Sep. 2000.

[42] L. Ferro-Famil, Y. Huang, and A. Reigber, "High-resolution SAR tomography using full rank polarimetric spectral estimators," in *Proc. IEEE Int. Geosci. Remote Sens. Symp.*, Jul. 2012, pp. 5194–5197.

[43] V. Cazcarra-Bes, M. Pardini, M. Tello, and K. P. Papathanassiou, "Comparison of tomographic SAR reflectivity reconstruction algorithms for forest applications at L-band," *IEEE Trans. Geosci. Remote Sens.*, vol. 58, no. 1, pp. 147–164, Jan. 2020.

[44] K. P. Papathanassiou and S. R. Cloude, "The effect of temporal decorrelation on the inversion of forest parameters from pol-InSAR data," in *Proc. IEEE Int. Geosci. Remote Sens. Symp.*, vol. 3, Jul. 2003, pp. 1429–1431.

[45] M. Lavalle, M. Simard, and S. Hensley, "A temporal decorrelation model for polarimetric radar interferometers," *IEEE Trans. Geosci. Remote Sens.*, vol. 50, no. 7, pp. 2880–2888, Jul. 2012.